# Thermal Annealing of Polymer Nanocomposites via Photothermal Heating: Effects on Crystallinity and Spherulite Morphology

Vidya Viswanath,[†] Somsubhra Maity,[‡] Jason R. Bochinski,[‡] Laura I. Clarke,*[,‡] and Russell E. Gorga*[,†]

[†]Fiber and Polymer Science Program, North Carolina State University, Raleigh, North Carolina 27695, United States
[‡]Department of Physics, North Carolina State University, Raleigh, North Carolina 27695, United States

ABSTRACT: Metal nanoparticles embedded within polymeric systems can act as localized heat sources, facilitating in situ polymer processing. When irradiated with light resonant with the nanoparticle's surface plasmon resonance (SPR), a nonequilibrium electron distribution is generated which rapidly transfers energy into the surrounding medium, resulting in a temperature increase in the immediate region around the particle. This work compares the utility of such photothermal heating versus traditional heating in gold nanoparticle/poly(ethylene oxide) nanocomposite films, crystallized from solution and the melt, which are annealed at average sample temperatures above the glass transition and below the melting point. For all temperatures, photothermally annealed samples reached maximum crystallinity and maximum spherulite size faster. Percentage crystallinity change under conventional annealing was analyzed using time–temperature superposition (TTS). Comparison of the TTS data with results from photothermal experiments enabled determination of an "effective dynamic temperature" achieved under photothermal heating which is significantly higher than the average sample temperature. Thus, the heterogeneous temperature distribution created when annealing with the plasmon-mediated photothermal effect represents a unique tool to achieve processing outcomes that are not accessible via traditional annealing.
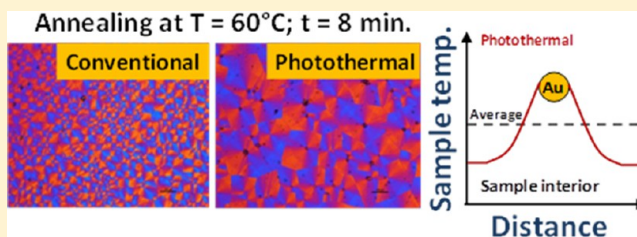
I. INTRODUCTION

The macroscopic properties of semicrystalline polymers are determined by structural morphology at the molecular level, including crystallinity fraction and crystallite size and structure. Postfabrication thermal annealing at temperatures significantly above the polymer glass transition T_g (but below the melt temperature T_m) is a straightforward, efficient approach to alter nanoscale molecular organization and realize improvements in bulk properties due to increase in crystal size and perfection.[1−3] Annealing increases crystallinity by aiding both nucleation and, particularly importantly, growth of spherulitic superstructures which contain crystal lamellae.[4] Mechanical modulus and overall strength are improved due to reduction in the degree of molecular randomization.[5,6] Tuning polymer crystallinity also alters optical,[7,8] barrier,[9] and dielectric[10,11] properties as well as the percolation process in polymer nanocomposites, which are important parameters for applications such as controlled drug delivery,[12] biosensors,[13,14] energy storage devices,[15] and packaging.[16]

Annealing relies on a balance between thermally induced molecular motion, which reorganizes amorphous material or less-perfect crystals into larger or more perfect crystalline structures and bulk melting, which destroys existing crystalline regions. Ideally, to maximize crystalline fraction, existing highly stable crystalline regions should remain unchanged during the annealing process with only less stable (i.e., lower melting point) crystals or amorphous material (which has dynamics determined by $T − T_g$) experiencing thermally induced

changes. For this reason, the maximum crystallinity achievable is generally obtained by annealing at temperatures well below T_m (i.e., ∼10−20 °C).[17] However, from a practical processing perspective, for lower annealing temperatures, longer times are required to achieve maximum crystallinity. This observation argues that a heterogeneous temperature distribution, where the polymer is simultaneously subjected to a range of temperatures (randomly distributed throughout its interior), may be beneficial in manipulating crystallinity fractions if the average molecular mobility rate can be enhanced while simultaneously preventing bulk melting.

We explore this hypothesis in a metal (gold) nanoparticle: poly(ethylene oxide) (AuNP:PEO) nanocomposite film. Nanoparticles have previously been utilized for a wide range of technological applications including biological spectroscopy and imaging,[18,19] biochemical sensors,[20] and as nanoscale electronic components.[21−24] Here the photothermal property of metal nanoparticles embedded in a material environment is utilized: when the films are uniformly irradiated with visible light, the dilute concentration (1.6 wt %, 0.07 vol %) of metal nanoparticles provides local nanoscale-sized heat sources from which annealing of the polymer matrix occurs.

The photothermal effect of metal nanoparticles refers to surface plasmon resonance (SPR)-mediated heating, wherein

incident light energy is converted to heat.[25] The light absorbed by the nanoparticle generates a nonequilibrium electron distribution (i.e., a surface plasmon) that decays by electron–electron scattering.[26] The heated electron gas cools rapidly by exchanging energy with the nanoparticle lattice,[27] and the particle temperature increases significantly, leading to heating of the local environment. Under steady-state conditions, a temperature gradient (decaying as $\sim 1/\kappa r$ where κ is the thermal conductivity and r is the radial distance from the particle)[28−30] is established around each particle which is warmest near the particle and terminates at an average background temperature far from the particle. In the experiments described here, there is no specific interaction between the polymer and the incident light so when the sample is uniformly illuminated, absorption of the light, and thereby the photothermal heating, occurs only at particle locations.

The fundamental photothermal properties of metal nanoparticles have been previously scientifically explored and utilized in the aqueous phase,[31−38] particularly for hyperthermia-based cancer treatment,[39−44] and only recently has photothermal heating been applied to a solid medium or for materials processing, with a particular focus on drug delivery and actuation of shape memory polymers.[45−47] Recent published work has utilized photothermal heating to demonstrate wavelength[48,49] and polarization-specific[50] processing, with the ability to selectively thermally treat one subset of a sample and leave the remainder unchanged. The spatial specificity of particle-based heating enables energy to be deposited inside the polymeric medium as opposed to conventional methods where the outer surface heats first; thus, photothermal heating avoids potential surface melting before the interior warms, which is particularly important for thermally sensitive polymeric nanostructures.

In the current report, we compare the effect of postfabrication annealing with either photothermal heating or a conventional uniform-temperature approach at several different temperatures and a wide range of times, investigating the resulting structural morphology and crystallinity fraction as observed by polarized optical microscopy (POM) and differential scanning calorimetry (DSC). These measurements demonstrate that when annealing AuNP:PEO nanocomposites (initially crystallized from either solution phase or melt phase), the maximum crystallinity is achieved much more quickly when heating photothermally. This result is consistent with a heterogeneous temperature distribution within the sample where the regions near a nanoparticle (AuNPs are separated by an average distance of ~ 248 nm) are much warmer than the average temperature. In the experimental range ($T_m - 35\ °C$ to $T_m - 5\ °C$), our observations from conventional heating followed time–temperature superposition, enabling use of this calibration to estimate the "effective dynamic temperatures" when undergoing photothermal heating, which are significantly greater ($\sim 20\ °C$) than the average sample temperature. Thus, the rate at which crystallinity increases (and thus the time required to anneal) acts as though the sample were at a significantly higher temperature. This effect has special significance at average annealing temperatures close to T_m wherein photothermal annealing was found to produce effective temperatures significantly higher than the melting temperature, enabling higher temperature dynamics within the sample (i.e., a fast increase in crystallinity) without bulk sample melting which would occur under traditional annealing where the entire sample would uniformly experience the higher temperature.

This unusual approach to annealing may be particularly useful for nanostructured samples (such as electrospun nanofibers, nanopillars, or nanocolumns), enabling rapid crystallinity enhancement at the molecular scale without destroying desired mesoscale patterning. We utilize a time–temperature superposition model to understand the fundamental response of the polymer to heterogeneous internal temperatures and estimate an effective temperature near the nanoparticle heaters.

II. EXPERIMENTAL SECTION

II.1. Polymer Nanocomposite Fabrication. Citrate-stabilized gold nanoparticles (AuNP) were synthesized using the Frens method.[51] Aqueous tetrachloroauric(III) acid was reduced with aqueous trisodium citrate solution (both Sigma-Aldrich) to obtain spherical gold nanoparticles. Dry polyvinylpyrrolidone (PVP) (Scientific Polymers Products, Inc.) in an amount equal to that of the tetrachloroauric(III) acid was added to the solution to further stabilize the nanoparticles after synthesis. Freshly prepared nanoparticle solution was drop cast onto copper grids (Ted Pella, PELCO 400 mesh grids) for transmission electron microscopy (TEM) (Hitachi HF2000 transmission electron microscope), which showed approximately spherical particles with an average diameter of 24 ± 7 nm (Figure 1b). Extinction spectra of the solution were measured with
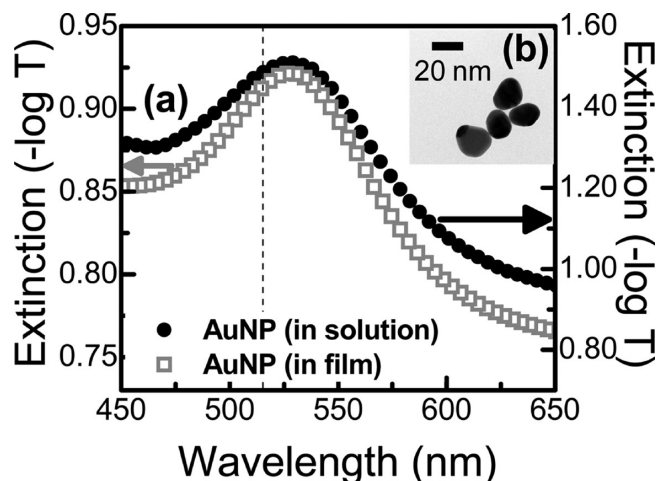

Figure 1. (a) Extinction spectrum of the nanocomposite film (left axis) and the gold nanoparticles (13 wt %) in aqueous solution (right axis), where the broad peak is the spectral location of the surface plasmon resonance (SPR). The vertical dotted line indicates the wavelength of the photothermal heating laser. (b) TEM image of neat gold nanoparticles.

an ultraviolet–visible spectrometer (CARY 50 Scan) to identify the location of the surface plasmon resonance (SPR) as 527 nm (Figure 1a), where the spectral location of the 514 nm photothermal excitation source (Coherent Sabre Innova) is indicated by the vertical dotted line.

For films crystallized from solution, PEO (molecular weight 400 000 g/mol) (Scientific Polymers Products, Inc.) was dissolved in deionized water to obtain a 6 wt % solution, which was combined with aqueous nanoparticle solution and perylene in powder form (Sigma-Aldrich # 394475-1G), resulting in 1.6 wt % AuNP:PEO and 0.09 wt % perylene:PEO in the final nanocomposite sample. The perylene additive enables internal temperature monitoring (see section II.2). The mixture was magnetically stirred for 10 h at room temperature and then spun cast (Laurell Technologies WS-650SZ-6NPP/lite) at 1000 rpm for 30 s on 2.5 cm × 2.5 cm glass slides (Fisherbrand, microscope cover glass 12-540B). Film thickness was measured by an alpha step profilometer (VeecoDektak Model 150) to be $11 \pm 2\ \mu m$. Extinction measurements (Figure 1a) confirm a negligible spectral

shift of the AuNP SPR in solution versus in the solid phase, indicating well-dispersed nanoparticles within the final nanocomposite samples. In order to compare annealing effects on melt-crystallized films, initially spin-coated film samples were subsequently heated at 64 °C for 15 min on a temperature-controlled heating stage and then cooled to room temperature under ambient conditions over 30 min (~1.5 °C/min). While neat PEO films typically appear whitish and translucent, samples containing the nanoparticles have a pinkish hue, consistent with absorption of the green portion of the visible spectrum and scattering of the red portion. Nanocomposite film samples were stored in the dark after fabrication until use.

II.2. Annealing Methods and Temperature Measurement. Conventionally annealed control samples were created utilizing a programmable, temperature-controlled heated stage (a copper block 2.5 cm × 7.5 cm × 1 cm attached to a commercial hot plate (VWR 7 × 7 CER hot plate)) as shown in Figure 2a. Samples were placed on the

(a) **Conventional Heating**

(b) **Photothermal Heating**
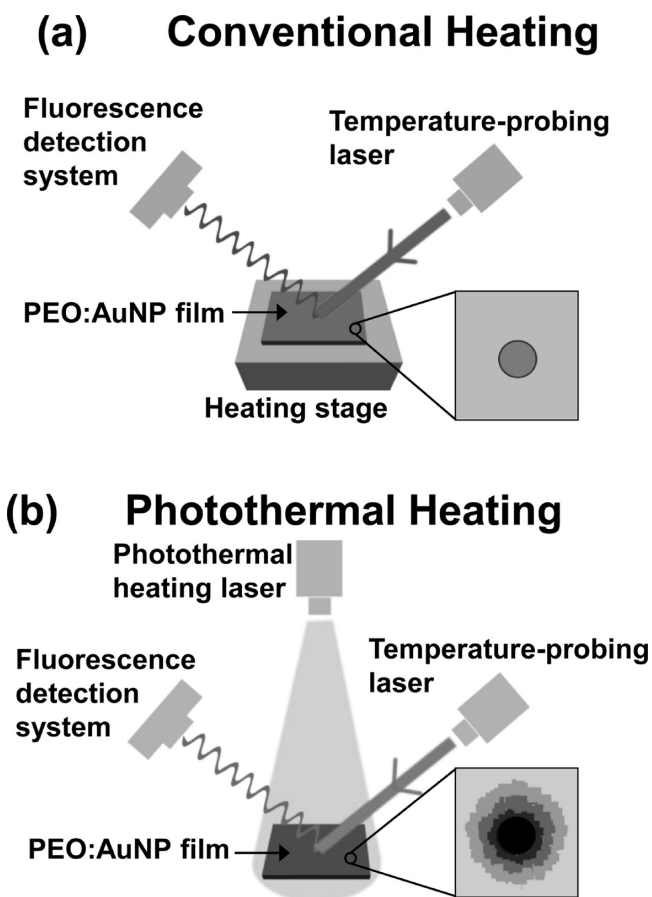
Figure 2. Schematic of (a) conventional and (b) photothermal annealing methods. Magnified diagrams of the nanocomposite sample are shown, schematically showing a gold nanoparticle remaining inactive in conventionally annealed, uniformly heated samples, and acting as a nanoscale heater due to SPR-resonant laser exposure in the photothermally annealed samples.

preheated stage, and the average temperature (which matched the calibrated set point of the hot plate) was monitored via a fluorescence technique during initial heat-up, the active annealing time at a constant temperature, and the cooldown to room temperature. Ramping temperature control matched the heating rate for conventionally heated samples to that which occurred for the photothermally annealed samples. Thus, for instance, for a 20 min anneal at 50 °C (Figure 3), the sample was heated at a rate of 2.5 °C/min for 10 min, held at 50 °C for 20 min, and then cooled at a rate of 1.7 °C/min for 15 min; hence, the temperature cycle matched for both the traditional and the photothermal cases.
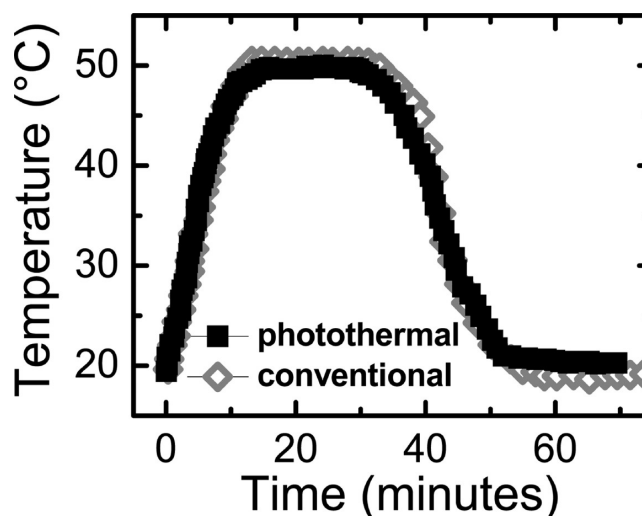

Figure 3. Identical heating and cooling curves (measured via perylene thermometry) for the samples during photothermal or conventional annealing for 15 min anneal at a temperature of 50 °C.

For photothermal annealing, samples were mounted on the same stage at room temperature and irradiated with 514 nm light, expanded to a spot size of 3 cm in diameter as shown in Figure 2b. The intensity of the laser beam was determined using a power meter (Coherent Model Powermax PM10). The average temperature of the system was increased by increasing the intensity of the laser, as discussed in detail previously.[49] In this work, light intensities ranging from 0.078 to 0.125 W/cm^2 were utilized, resulting in steady-state temperatures of 40 ± 2.4 to 60 ± 1.8 °C. Samples that had experienced photothermal annealing cooled significantly more slowly (~3× slower) than conventionally annealed samples after the heating source was removed. In order to exactly match the entire temperature cycle (heating and cooling), the cooling rate for photothermal annealing was matched to that observed under conventional annealing by applying an external cooling fan (Figure 3). If photothermally annealed samples are allowed to cool naturally from an annealing temperature of 50 °C, the time to reach maximum crystallinity decreases by ~20 min (data not shown) when compared to samples cooled using the external fan (data presented below). Thus, matching the entire temperature cycle enables isolation of the effect of the heterogeneous temperature alone; the increase in speed to maximum crystallinity is even greater without this control, as a slower cooling rate (i.e., a longer cooling time) is associated with higher crystallinity.

The solution crystallized films were annealed at 40, 50, and 60 °C by photothermal annealing and at 40, 45, 50, 55, and 60 °C by conventional annealing for times ranging from 4 to 400 min. The melt-crystallized films were similarly annealed at 30, 40, 50, and 60 °C for durations ranging from 4 to 160 min.

A noncontact measurement using the fluorescent molecule perylene was used to monitor the average temperature of the nanocomposite.[52] Perylene has multiple emission wavelengths and the shape of this emission spectrum changes with temperature (Figure 4). In particular, the ratio of the emission intensity at the "trough" at 465 nm to that of the "peak" at 479 nm is essentially linear with temperature (where a calibration curve is determined using conventional heating) as shown in Figure 4 (inset); hence, observing the perylene fluorescence provides an in situ probe of temperature, as described previously.[49]

A 405 nm, 5 mW continuous-wave violet diode laser was amplitude-modulated at a rate of 2 kHz, expanded to a spot size of 0.5 cm diameter, and aligned on the sample spatially overlapping the photothermal heating laser. The corresponding fluorescence spectrum was imaged onto the entrance slit of a double-grating scanning monochromator (SPEX 1680B) with a side-on photomultiplier tube (PMT) detector (Hamamatsu 931B) at the exit port. The amplified
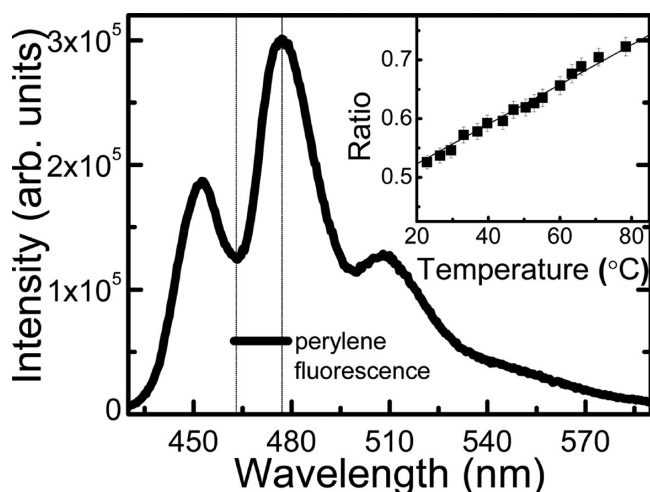
Figure 4. Full emission spectrum of embedded perylene at 25 °C; vertical lines indicate spectral locations of the peak and trough used for temperature measurement. Inset: ratio of perylene emission intensity under conventional heating enables calibration of the fluorescence–temperature relationship.

PMT output was photon-counted (Stanford Research Systems SR400), with a corresponding background correction.

Perylene is dispersed uniformly at a dilute level (0.09 wt %, 0.02 vol %) within the polymer nanocomposite. Because of the large average distance between gold nanoparticles, ~248 nm (derived from a polymer: nanoparticle concentration calculation), the majority of the perylene molecules are located far from a nanoparticle. This result can be demonstrated from a simple model: dividing the average distance between two particles into three equal radial segments, the total volume of material associated with each particle (i.e., a sphere of radius 124 nm with a total volume of 7.99×10^{-21} m^3) divides into a sphere closest to the sample with radius 41 nm (volume 2.88×10^{-22} m^3), a spherical shell with radii between 41 and 82 nm (volume 2.02×10^{-21} m^3), and a second spherical shell with radii between 82 and 124 nm (volume 5.68×10^{-21} m^3). The warmest regions of the sample will be within the spheres most closely surrounding the nanoparticle which represent only 3.6% of the total sample volume. Assuming the perylene molecules are uniformly distributed, this model indicates that the warmest regions will contribute less than 4% of the measured perylene signal. Moreover, the overall perylene quantum efficiency actually decreases by ~20% with increasing temperature over the range employed here (i.e., the total fluorescence will have an even smaller contribution from the warmest regions). Thus, it can be inferred that the perylene measures the "average" temperature of the system with only a ~3% contribution coming from the hottest regions nearest to the nanoparticles.[30]

II.3. Sample Characterization. Polarized optical microscopy (POM) was employed to study spherulite morphology in the polymer nanocomposite films. Using a Nikon Eclipse 50i POL optical microscope at 100× and 400× magnification, micrographs of the control and annealed films were captured with a CCIDIRIS/RGB color video camera (Sony Corporation), using crossed polarizers and a first-order wave plate (λ = 530 nm). Because of the anisotropy of the spherulite, when viewing a sample under crossed polarized light, the spherulitic structure (chains of the crystallites oriented either perpendicular or parallel to the spherulite radius) results in a specific arrangement of the optical indicatrices. This results in the formation of a Maltese cross pattern which arises from the interaction of polarized light with the crystallites within the sample.[53] The light emerging from a first-order wave plate remains linearly polarized yet is retarded by 530 nm, which can be used to calculate the birefringence but is utilized here to provide an additional means of contrast (due to the color gradient) between adjacent spherulites during image analysis. Difference in color of polarized images can be attributed to

birefringence changes arising from differences in the surface structure/thicknesses of the films.

Spherulite density (number of spherulites per volume) was calculated by counting the number of spherulites per unit area from the polarized optical micrographs and accounting for the known film thickness. Similar approaches to determine nucleation densities have been previously reported.[54−56] Images were processed using the split channel mode to separate the red, green, and blue components (using the NIH ImageJ software). The component with the best contrast showing clearly discernible spherulite boundaries was selected, and spherulite number was determined using the point selector tool to prevent repetitive counting. At least two separate images were analyzed for each annealing condition. Quantitative analysis was not performed for conditions where spherulite boundaries were not discernible due to morphology changes (e.g., such as the transformation to a hedritic structure).

Differential scanning calorimetry (DSC) was performed using a PerkinElmer Diamond DSC-7 to determine the crystalline fraction. The specimens were subjected to heating scans from 25 to 80 °C at a heating rate of 5 °C/min (first heating cycle). Pyris software was used to analyze the DSC data. Overall sample crystallinity percentage (% X_c) was calculated by % $X_c = (\Delta H_m / \Delta H^*_m) \times 100$, where ΔH_m and ΔH^*_m are the melting enthalpies for the specimen and 100% crystalline PEO, respectively (ΔH^*_m = 213.7 J/g).[57] Crystallinity calculations via DSC were confirmed using wide-angle X-ray diffraction for the PEO/AuNP control (58% and 56%, respectively). Wide-angle X-ray diffraction was performed using a Rigaku Smartlab diffractometer with Cu Kα radiation (λ = 0.1541 nm).
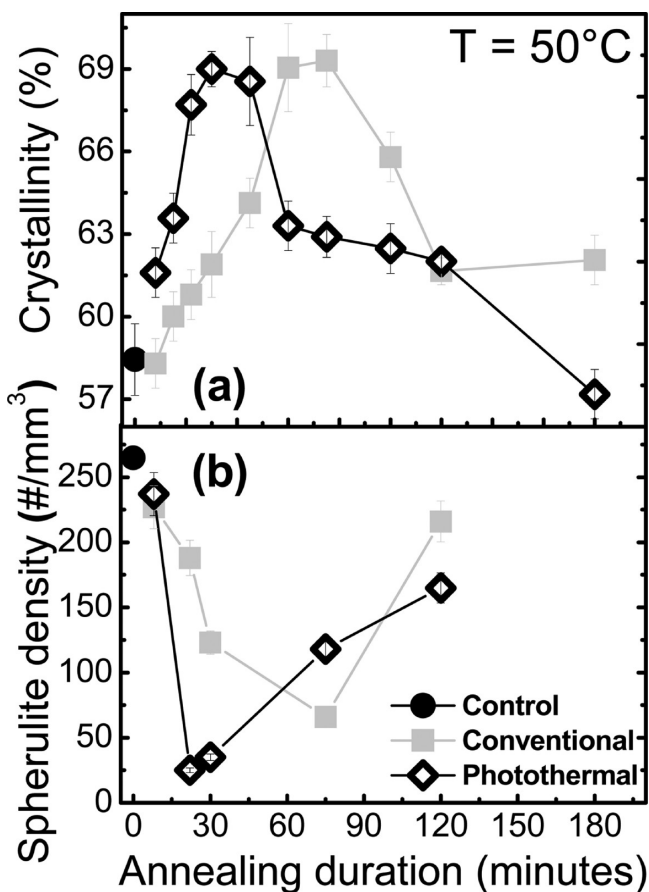
III. RESULTS AND DISCUSSION

III.1. Effect of Presence of Nanoparticles and Brief Background. The AuNP:PEO nanocomposites overall exhibited a similar range of crystallinity values as neat PEO films, indicating that the addition of a low concentration of particles did not significantly enhance or inhibit the ability of PEO to crystallize. As originally fabricated, AuNP:PEO films have a crystallinity fraction of 58 ± 1%, comparable with the value of 60 ± 1% in neat PEO. No pronounced change in peak melt temperatures (T_m) was observed, with T_m in the range of 64−67 °C for both neat PEO and composite films. These crystallinity and T_m values are consistent with those reported for similar systems of PEO composites with gold nanoparticles.[58] The maximum crystallinity observed in the PEO composite films used in this study was ~70%, consistent with expectations for an entangled semicrystalline PEO obtained in previous studies.[59,60]

The nanocomposite films revealed the distinct presence of spherulitic morphology as shown in the optical microscopy images in the figures throughout this work. Spherulites are spherical structures formed during crystallization of polymers under quiescent conditions, which include radial protrusions that alternate between crystalline regions (where lamellae are the dominant structure) and regions of amorphous chains. After nucleation, lamellae grow radially outward from the nucleation site but the entanglement of the polymer chains traps amorphous materials between these crystalline regions. Postprocessing annealing of films has been associated with both new nucleation/growth and growth of existing spherulites.[61] Annealing increases the size of the spherulites by providing the thermal energy necessary for continued radial growth of lamellae.[62,63] Previous studies have demonstrated that annealing PEO films at temperatures close to the melt temperature (for sufficient time) results in crystal melting and subsequent recrystallization.[64,65] This overt melting process produces a new crystallization pattern determined by the conditions present

during recrystallization; in this work, melting and recrystallization resulted in a decrease in crystallinity fraction.

Since irradiated gold nanoparticles provide the source of heat in photothermal annealing, efforts were taken to ensure that the nanoparticles were dispersed uniformly throughout the nanocomposite film. When nanoparticle aggregation occurs, the surface plasmon resonance shifts to redder (i.e., longer) wavelengths.[66] Figure 1 compares the SPR for nanoparticles well-dispersed in solution and in the polymer composite, where the similar spectral location of SPR indicates that the nanoparticles are remain isolated and do not aggregate within the solid film. PEO lamellae in spherulitic morphologies possess thickness of 10−15 nm,[67,68] whereas the characteristic size of the nanospheres utilized in this work is 24 ± 7 nm. Thus, by steric hindrance it is expected that the nanoparticles remain in the amorphous regions of the semicrystalline polymer nanocomposite system. Such locating of particles may assist in enhancing crystallization by usefully generating the photothermal heat selectively in the amorphous regions.

III.2. Annealing of Solution Crystallized Films. Figure 5a displays the change in crystallinity in AuNP:PEO nanocomposite films as a function of annealing time at 50 °C (i.e., $\sim T_m - 15$ °C) under uniform heating (e.g., the conventional approach) versus heterogeneous heating via the photothermal effect of the embedded gold nanoparticles. In both cases, the

crystallinity was found to increase initially and then decrease at longer durations of annealing. This general trend can be explained as follows. At short times, the dominant effect is the conversion of amorphous or mesophase material to crystalline and growth of spherulites (discussed below); however, at longer times, crystal melting and recrystallization occur. Recrystallization after melting results in lower overall crystallinity as the recrystallization process occurs in a completely different environment than the initial condition (i.e., crystal formation as solvent is lost during initial film fabrication). As discussed below, after melting, many small spherulites are observed. At lower processing temperature (where bulk melting cannot occur during the time scale of the experiment, <35 °C, data not shown) the crystallinity fraction saturates at long times. Reduced crystallinity at longer annealing times has been previously reported for other semicrystalline polymeric systems.[69,70]
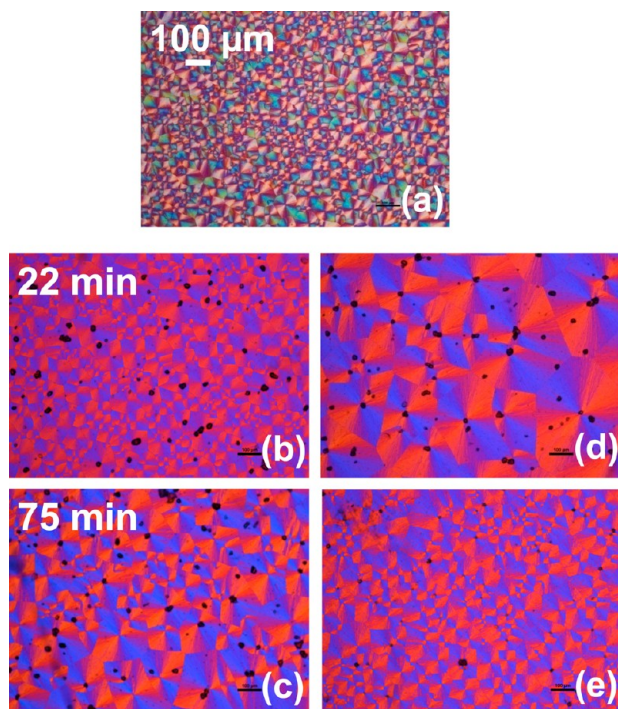
The perfection/growth of crystals at short times and overt melting at longer times is one example of the effect of time−temperature superposition where a barrier-limited process (here both reorientation of segments within amorphous material to enable crystal formation and melting) can occur either due to increased temperature or increased time.[71]

Though the bulk average temperature is the same under both annealing protocols and the general shape of the response is similar, the photothermally annealed films show a much faster increase in crystallinity (maximum value at 33 min) as compared to conventionally annealed films (maximum value at ∼68 min). Thus, the heterogeneous temperature distribution results in a faster response.

The increase in crystallinity can be correlated with changes in spherulite size by imaging the spherulites as shown in Figure 6. Spherulite density (i.e., number per volume) from analysis of different images taken as a function of time is shown in Figure 5b. Spherulite density is a minimum (i.e., the spherulite size is a maximum) at similar annealing times as when the crystallinity fraction is maximized. The largest spherulites are obtained for significantly shorter annealing times (22 min) under photothermal annealing as compared to the traditional approach (>75 min). Following the trends shown in the crystallinity fraction, at long times the spherulite diameter decreases as melting destroys the existing structure and new smaller spherulites are nucleated from the melt upon cooling to room temperature. This decrease in spherulite size (associated with melting) does not occur when annealing at low temperatures (e.g., 30 °C for 2700 min) where melting cannot occur during the time scale of the experiment.

Figure 7 shows the effect of annealing at 60 °C (i.e., $\sim T_m - 5$ °C). The general trends (crystallinity increase and then decrease) shown at lower temperatures similarly occur but at shorter times. Furthermore, photothermally annealed samples achieve overall higher crystallinity values (71 ± 2%) than results from conventionally annealing (65 ± 1%) in approximately 20% of the time (8 min versus 37 min). Again, spherulite density from optical images as a function of annealing time shows similar trends as at lower temperatures (Figure 8). While it takes 30 min of conventional annealing to produce the largest spherulites (Figure 8c), it takes only 8 min to achieve the largest spherulite size (corresponding to maximum crystallinity) via photothermal annealing (Figure 8e).

At longer annealing times at 60 °C (>20 min for photothermal and >45 min for conventional), significant morphological changes were observed (Figure 9): instead of


Figure 5. Sample crystallinity measured by DSC as a function of annealing time at 50 °C (i.e., at $\sim T_m - 15$ °C) for films of PEO doped with 1.6 wt % of gold nanospheres annealed via photothermal (open diamonds) or conventional (gray squares) methods. The control is an untreated sample as fabricated. (b) Spherulite density (number of spherulites per unit volume) as a function of annealing time.

Figure 6. Cross-polarized optical images of (a) as-spun AuNP:PEO films; after conventional annealing for (b) 22 and (c) 75 min; and after photothermal annealing for (d) 22 and (e) 75 min at 50 °C.


Figure 7. (a) Crystallinity and (b) spherulite density as a function of annealing duration for AuNP:PEO films postprocessed via conventional and photothermal heating at 60 °C.

spherulites of decreasing size (as the maximum in crystallinity has already been achieved), an intermediate spherulite−hedrite morphology was observed. Note: spherulite densities are not reported once a disruption of the spherulite morphology is observed. Hedritic morphology has previously been reported in PEO during annealing studies.[61,72−75] Hedrites are composed of a number of lamellae joined together along a common line or, more often, along a common plane. Whereas hedrites are mainly layered lamellar structures grown from a central screw dislocation, spherulites are lamellar structures that grow in three dimensions.[73]

Figure 9a is an image of spherulitic structures (shown at the peak of the crystallinity after an 8 min photothermal anneal at 60 °C), which develops into an intermediate semihedritic morphology after a 22 min (Figure 9b), until (after 30 min) becoming a hedritic structure with a complete absence of spherulites and showing the presence of internal dominant lamellar structure (Figure 9c). Intermittent featureless patches outside of the hedritic structure are observed (Figure 9b), indicative of annealing-induced partial melting which is responsible for thermal etching of the previously formed spherulitic structure, thereby producing a hedrite with underlying lamellae exposed. These images support the hypothesis that the samples melt given sufficient annealing time with complete destruction of the spherulites initially formed from solution crystallization and subsequently enhanced by short-time annealing.

Both conventional and photothermal annealed samples showed the hedritic morphology with the process arising at earlier annealing times under photothermal heating. Thus, such morphology is a natural result of annealing PEO near T_m and as with other crystallinity changes simply occurs more rapidly
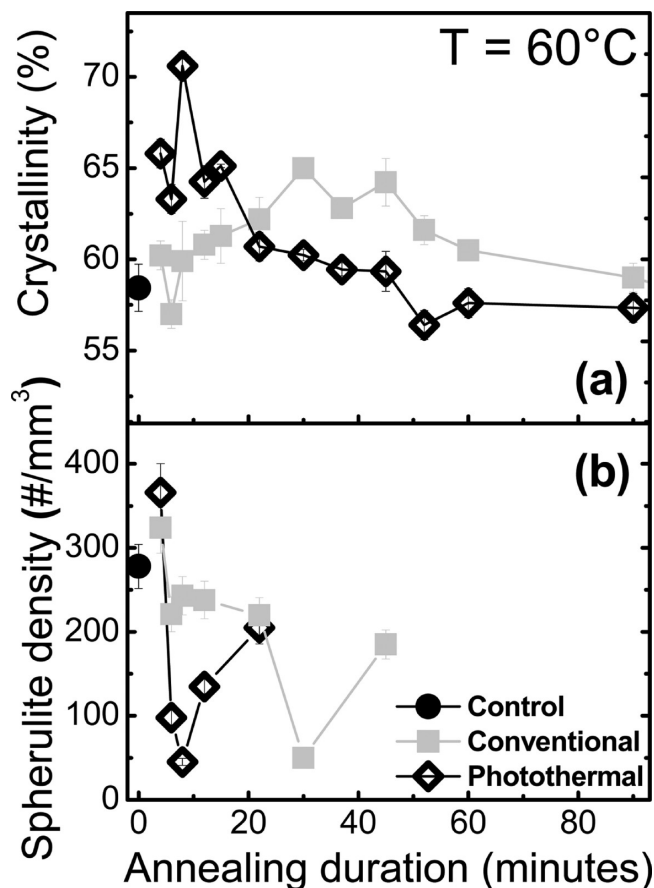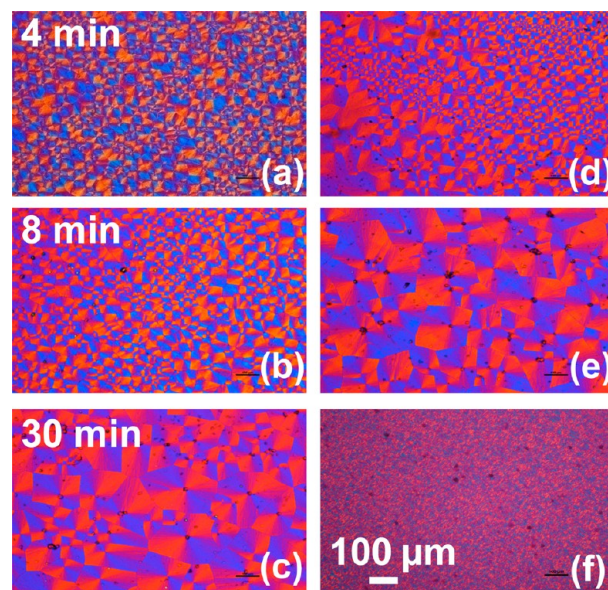
Figure 8. Cross-polarized optical images of the AuNP:PEO films after annealing at 60 °C for 4, 8, and 30 min conventionally (a, b, c) and photothermally (d, e, f), respectively.

under photothermal heating. This argues that the innate crystallization process in PEO is unchanged with the addition
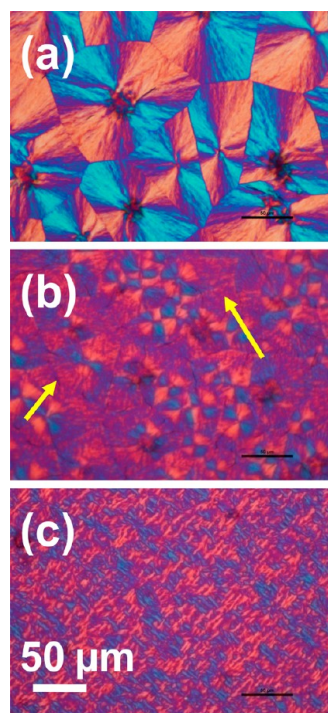
Figure 9. Cross-polarized optical images of the AuNP:PEO films after photothermal annealing at 60 °C for (a) 8 min, (b) 22 min, and (c) 30 min reveal the transition from spherulitic to hedritic morphology. The yellow arrows indicate regions of intermittent melting.

of the AuNP and the resultant morphology achieved via photothermal annealing is similar to that obtained by conventional heating for longer times. The only exception to this rule is the higher crystallinity fraction obtained at $T_m - 5$ °C via photothermal heating, which appears to be unachievable by conventional heating at any time.

Table 1 summarizes the annealing time required to obtain maximum crystallinity (from DSC) and the average annealing

Table 1. Annealing Time to Maximum Crystallinity and to Obtain Largest Spherulites (Minimum Spherulite Density) in Solution Cast Films for Different Annealing Temperatures Using Conventional or Photothermal Annealing

annealing temp (°C)	annealing technique	annealing time to max crystallinity (min)	av time to min spherulite density (min)	max crystallinity (%)
40	conventional	200 ± 14	180 ± 20	64 ± 1
	photothermal	55 ± 7	45 ± 15	68 ± 1
45	conventional	180 ± 14	180 ± 14	67 ± 1
50	conventional	68 ± 11	75 ± 15	69 ± 1
	photothermal	33 ± 16	22 ± 8	69 ± 1
55	conventional	55 ± 7	60 ± 15	70 ± 2
60	conventional	37 ± 10	30 ± 7	65 ± 1
	photothermal	8 ± 4	8 ± 4	71 ± 2

time at which the largest spherulites (minimum spherulite density) are obtained (from polarized light microscopy) for different conventional (5) and photothermal (3) annealing temperatures. From this data it is clear that photothermal annealing decreases the annealing time necessary to achieve the maximize crystallinity (and minimum spherulite density). Further for the lowest and highest annealing temperatures

reported (40 and 60 °C, respectively) there is a statistically significant increase (albeit small) in the crystallinity for the samples annealed photothermally.
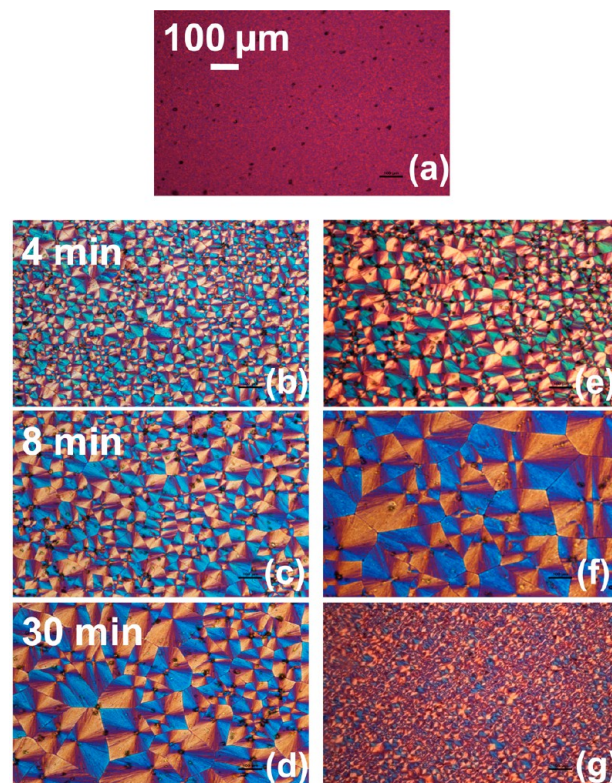

Figure 10. Cross-polarized optical images of (a) melt-crystallized AuNP:PEO film after conventional annealing at 60 °C for 4, 8, and 30 min conventionally (b, c, d) and photothermally (e, f, g), respectively.

III.3. Annealing of Melt-Crystallized Films. Figure 10 shows the effect of annealing films crystallized from the melt (solution-cast films heated to 65 °C for 15 min, which results in complete melting) and then cooled to room temperature under ambient conditions (~30 min cool) at 60 °C. Melt-crystallized samples had a lower crystallinity fraction (54 ± 1%) than solution-crystallized films (58 ± 1%) and, as fabricated, showed no clear evidence of either hedrite or spherulite morphology, although lamella-like features may be discernible (Figure 10a).

Melt-crystallized films annealed at 60 °C show the development of crystalline structure, marked by well-formed spherulites as illustrated in Figure 10. Photothermally annealed samples revealed a faster development of spherulitic morphology, producing the largest spherulites at 8 min of annealing, as compared to conventional annealing where the largest spherulites occurred for 30 min times (as summarized in Figure 11b). Similar to solution crystallized films, at shorter annealing times, as the spherulites begin to grow the overall crystallinity increases, as shown in Figure 11a for the melt-crystallized films. At longer durations, melting occurs, which results in the nucleation and growth of new, smaller spherulites, thereby resulting in a decrease in crystallinity. These trends are observed at each annealing temperature investigated, presented in Table 2. As temperature increases, the annealing time required to reach maximum crystallinity decreases. The biggest spherulites (i.e., minimum spherulite density) occur at the same
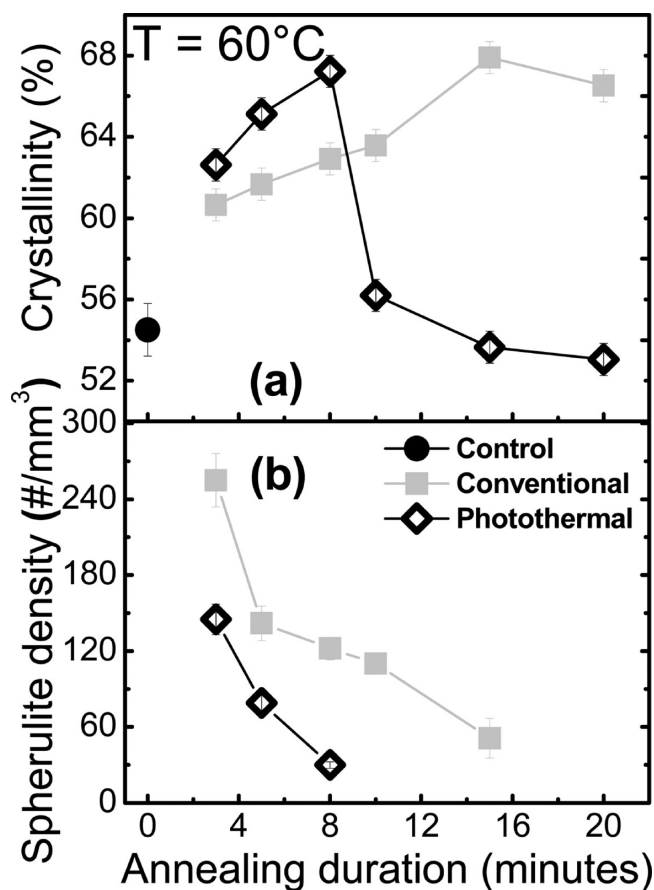
Figure 11. (a) Crystallinity and (b) spherulite density as a function of annealing time for AuNP:PEO melt-crystallized films annealed by conventional and photothermal heating at 60 °C. Quantitative analysis was not performed for conditions where spherulite boundaries were not discernible due to morphology changes (e.g., such as the transformation to a hedritic structure) (see Figure 10g).

Table 2. Annealing Time to Maximum Crystallinity and to Obtain Largest Spherulites (Minimum Spherulite Density) in Films Crystallized from the Melt at Different Annealing Temperatures Using Conventional and Photothermal Annealing

annealing temp (°C)	annealing technique	annealing time to max crystallinity (min)	av time to min spherulite density (min)	max crystallinity (%)
30	conventional	120 ± 41	150 ± 30	64 ± 1
	photothermal	90 ± 31	90 ± 30	65 ± 1
40	conventional	75 ± 10	90 ± 15	69 ± 1
	photothermal	30 ± 21	60 ± 15	66 ± 1
50	conventional	30 ± 10	30 ± 15	67 ± 1
	photothermal	15 ± 14	15 ± 7	68 ± 1
60	conventional	15 ± 2	15 ± 5	68 ± 1
	photothermal	8 ± 3	8 ± 3	67 ± 1

annealing time (for a given temperature), thereby confirming that the resultant crystallinity increase observed is due to the increase in spherulite size.

As summarized in Figures 11 and Table 2, the same trends observed for solution-crystallized samples are present in melt-crystallized samples. Photothermal heating increases the speed to the maximum crystallinity. Comparing the two types of films, the maximum crystallinity achievable at a given temperature

was independent of sample type and presumably set by the degree of entanglement within PEO of this molecular weight. However, it is germane to note that films crystallized from the melt reach the same maximum level of crystallinity more rapidly than solution-crystallized films. This may be due to steric effects: the large initial spherulite size in solution-crystallized samples hinders further spherulite growth due impingement of neighboring spherulites; in contrast, the almost featureless morphology of the melt-crystallized films enables rapid initial growth before spherulite interactions become significant.

III.4. Time–Temperature Superposition. For annealing studies in general and this work in particular, the interplay between time and temperature led to the point of sample maximum crystallinity fraction. Specifically, the needed annealing time decreases with increasing temperature. Recently, time–temperature superposition has been applied to conventional polymer annealing,[76] where data at different temperatures were compressed into a master curve by shifting along the time axis. The time to reach maximum crystallinity at a given temperature, normalized by the same quantity at a single low reference temperature, was defined as a shift factor, and the scaling of such as a function of temperature was utilized to determine a characteristic barrier in the system. Because the effect of plasmonic heating is heterogeneous, there is no single temperature that describes the photothermal annealing process; however, by comparing photothermal shift factors to those from conventional heating, an "effective dynamic temperature" can be determined. That is, the system responds at a rate that is consistent with the effective dynamic temperature. This enables quantification of the effect of photothermal heating at the molecular scale.

Time–temperature superposition is associated with thermally activated processes where rates are generally exponentially dependent on the ratio of barrier height to temperature. Thus, motion or relaxation is possible at any temperature: one must simply wait long enough for a thermal fluctuation that overcomes the average barrier height in the system. In photothermal heating, only a small fraction of the sample, near the particle, experiences the higher temperature. However, because thermally activated processes are exponentially dependent on temperature, the effect of this minute fraction is observable, while the remainder of the sample is relatively cool. This heterogeneous heating approach appears to prevent bulk melting while enhancing the motion of amorphous or metaphase material, enabling it to crystallize; the location of the particles (primarily in the amorphous region due to steric effects) may enhance this effect. Our analysis below focuses on this simple model of thermal activation with a distribution of barriers.

To determine the shift factors (utilizing conventional heating where the temperature is known throughout the sample), the lowest available temperature was utilized as the reference value (40 °C (30 °C) for solution (melt)) crystallized samples since it is closest experimental temperature to the PEO glass transition temperature. (Experiments on solution-crystallized samples at 30 °C were inconclusive at times up to 2000 min.) The shift factor a_T, defined as the ratio of the experimental time to achieve maximum crystallinity to the same quantity at the reference temperature, is defined in eq 1 as

$$\ln(a_T) = A + \frac{E_a}{kT} \tag{1}$$

where the underlying dynamics in the system are assumed to fit a simple Arrhenius equation. In eq 1, E_a is the effective activation energy (average barrier height), k is the Boltzmann constant, T is the temperature, and $A = -E_a/kT_{ref}$ is a dimensionless constant where T_{ref} is the reference temperature.[77] Plots of $\ln(a_T)$ versus $1/T$ for conventional heating are shown in Figure 12a (b) for solution (melt) crystallized films
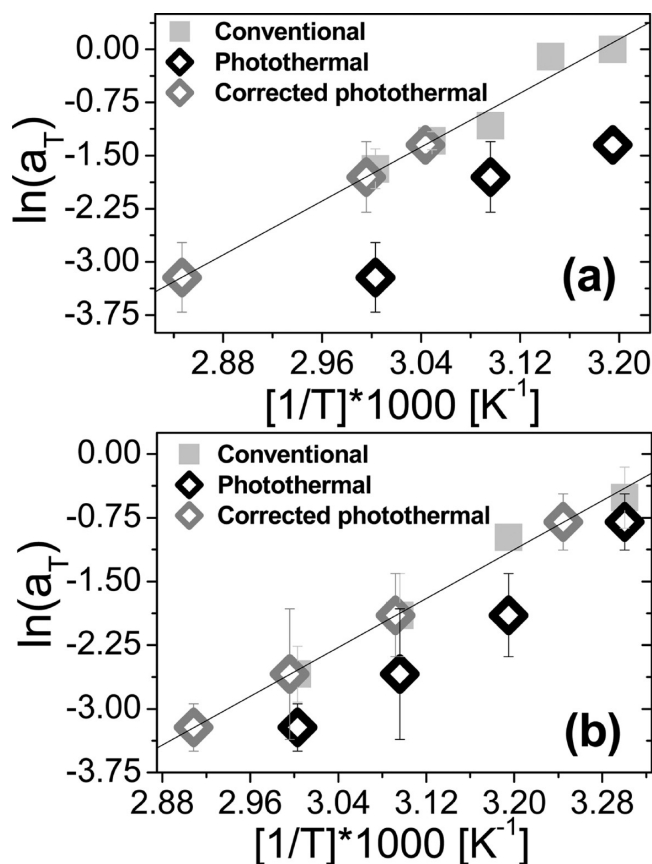
Figure 12. Logarithm of shift factor as a function of reciprocal temperature for films crystallized from (a) solution and (b) the melt for conventional or photothermal annealing. The solid lines show a linear regression through the conventional annealing data.

(filled squares). Over this temperature range, the Arrhenius fit is sufficient and produces a linear relationship between $\ln(a_T)$ and $1/T$ (where $E_a = 18.8$ kcal/mol and $A = -30.29$ for solution-crystallized films; $E_a = 14.3$ kcal/mol and $A = -24.16$ for melt-crystallized films). Observed shift factors for photothermal heating are also shown (open diamonds) initially plotted at the background temperature. In fact, as discussed above, the background temperature is not the effective temperature for photothermal annealing, as evidenced by the lower than expected time to maximum crystallinity, and thus *a priori*, this initial placement is incorrect. While the annealing process is the same (as argued above) in both cases (and thus a_T should be the same at a given temperature), the effective temperature at which the photothermal process occurs is higher than the average temperature experienced by both samples. Thus, by examining Figure 12, the actual effective temperature (the temperature at which the system is responding) can be determined by shifting the photothermal data onto the calibration curve determined by the conventional data; that is, the photothermal data (open black diamonds) are translated

horizontally until they fall on the linear regression curve (open gray diamonds). This calibration enables quantification of an effective dynamic temperature which is discussed below and depicted in Figure 13.
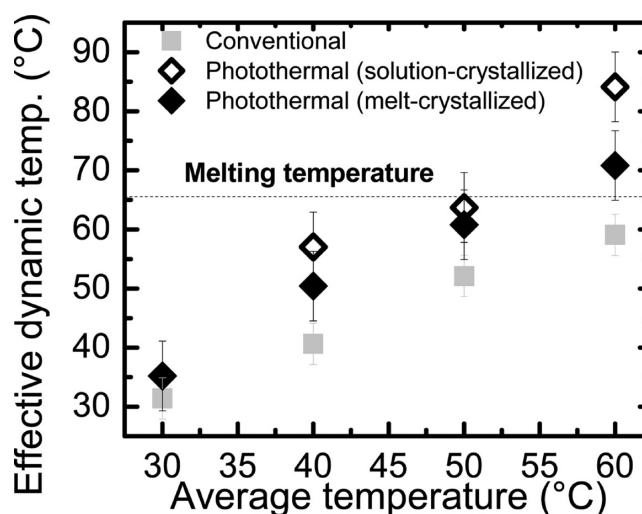
Figure 13. Effective dynamic temperature for AuNP:PEO films crystallized from either solution or melt and annealed at the average temperature.

Figure 13 shows the effective dynamic temperature obtained from time–temperature superposition plotted as a function of the average temperature. To reiterate, the average temperature is the temperature present at all locations under conventional annealing and far from the gold nanoparticles under photothermal heating. Even though the time–temperature superposition analysis resulted in a slightly different average barrier value (E_a) in the melt-crystallized and solution-crystallized cases (which reflects the different steric environments), the effective dynamic temperatures in the two cases are similar. Thus, regardless of the specific morphology, the PEO responded at a rate that was consistent with a temperature 5–25 °C higher than the background. For instance, for samples annealed photothermally at an average temperature of 50 °C, the time to reach maximum crystallinity indicates that the effective dynamic temperature is approximately 65 °C (for both solution and melt-crystallized samples). It is important to note that this cannot be achieved by conventional annealing, since annealing at 65 °C ($\sim T_m$) would result in complete melting of the crystal structure and subsequent melt crystallization upon cooling (similar to what is seen in the melt-crystallized films). Similarly, plasmonic heating at an average temperature of 60 °C resulted in effective dynamic temperature equivalent to heating at 70 °C (85 °C) for solution-crystallized (melt-crystallized) films, well above the melting temperature of the polymer. However, no visible melting of the sample is observed at times up to which the maximum crystallinity is observed ($\sim$8 min). In fact, a continuous and rapid increase in crystallinity is observed, evidenced by a steady increase in spherulite size, up to the annealing time for maximum crystallinity. This intentional breaking of the symmetry between melting and annealing (transitioning amorphous material to crystalline) may explain the higher maximum crystallinity possible under photothermal annealing at 60 °C ($T_m - 5$ °C).

As an aside, we point out that the temperature near the particle under photothermal heating is expected to increase at a

more rapid rate than the background temperature under these conditions, as discussed in other work.[30] Measurement of the effective temperature in the volume of polymer immediately surrounding photothermally heated gold nanorods in the same molecular weight PEO (with a similar AuNP:PEO ratio) in thin films slightly above the PEO melting point showed effective temperatures of 10−30 °C above the background temperature with this temperature difference increasing with laser intensity (and thus background temperature).

The results of Figure 13 indicate that heterogeneous heating via the photothermal effect breaks the symmetry between growth of lamella at the periphery of the spherulite and bulk melting of existing crystalline regions. If nanoparticles are dominantly positioned in amorphous regions, amorphous material will be more influenced by the annealing process. Furthermore, if the existing crystalline regions are the coolest in the sample, this will not only help to preserve existing crystalline structure but also serve as a cold nucleating site, triggering the warm amorphous material to crystallize. This temperature-induced symmetry break between melting and crystal formation is not possible in a uniformly heated sample.

To illustrate the potential utility in annealing with photothermal heating, Figure 14 shows the annealing time to achieve
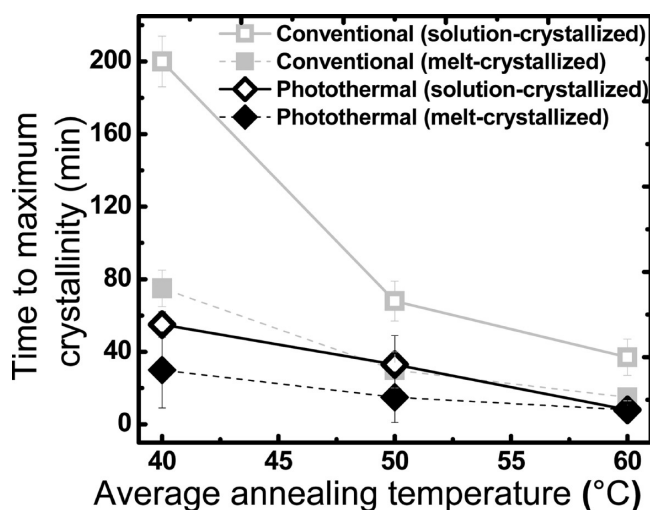
Figure 14. Time to reach the maximum crystallinity (t_{max}) as a function of average annealing temperature as determined by DSC for each annealing time at each temperature.

the maximum crystallinity (%) at a particular temperature (t_{max}) as a function of the average annealing temperature. Comparing conventional annealing of solution crystallized films (gray open squares/gray solid line) with the photothermally annealed films (black open diamonds/black solid line), it is evident that photothermal annealing has a lower t_{max} at every temperature. The same can also be seen in melt-crystallized films, for photothermally and conventionally annealed films (the black closed diamonds/black dotted lines and gray closed squares/gray dotted lines, respectively). Whereas at higher temperatures, as discussed in the previous paragraph, photothermal annealing enables access to processing regimes not accessible by traditional means, at low temperature, the photothermal approach has a significant practical advantage: much shorter annealing times. In fact, the difference in t_{max} is most pronounced at lower temperatures where the time required to achieve the maximum crystallinity (i.e., largest spherulites) is

3−6 times more rapid than that required for conventional annealing.

Thus, there are benefits to photothermal heating both far from and close to the melting temperature of the matrix polymer. Well below the melting point, photothermal heating allows annealing at lower average temperatures and for shorter times than that for a traditional annealing approach. At postprocessing temperatures close to T_m, photothermal heating effectively enables higher annealing temperatures than would be possible with traditional annealing. Thereby processing outcomes can be achieved with photothermal heating that are not accessible with traditional means.

IV. CONCLUSION

This work demonstrates the efficacy of photothermal heating as a tool for annealing metal particle polymer nanocomposite systems. At low annealing temperatures (relative to the melt temperature), photothermal annealing can be used to attain maximum crystallinity in shorter annealing times, while at temperatures closer to the melt, it produces effects akin to annealing at much higher temperatures, without globally melting the sample, thus generating results not attainable via traditional annealing schemes. This symmetry-breaking ability to perfect and grow existing spherulites while preventing bulk melting is due to the heterogeneous temperature distribution within the sample where the temperature increase is much larger in the regions around the nanoparticles than in the remainder of the sample. The effective dynamic temperature at which the sample responds was calculated via use of the time−temperature superposition principle.

This research extends scientific understanding of the use of metal nanoparticles as localized heat sources within solid (particularly polymeric) materials to manipulate crystallinity, cross-linking, or chemical reactions within a solid object upon exposure to visible light. In this postprocessing approach, internal sample structure can be altered at any point during an object life cycle: immediately after traditional fabrication (such as molding) to improve properties, to repair or reinforce during the active life of the object, or at end-of-use to trigger degradation. Although in this work, the metal nanostructures were introduced specifically for photothermal heating, the same approach could be utilized in any metal particle containing composite where the primary use of the particle was another function (e.g., thermal, electrical, or optical). As demonstrated here, the effects of the innately heterogeneous temperature distribution and avoidance of surface heating (due to heat being generated from inside the sample) enable access to new polymer processing outcomes that are not achievable via traditional thermal treatment.

■ AUTHOR INFORMATION

Corresponding Authors
*E-mail: liclarke@ncsu.edu (L.I.C.).
*E-mail: regorga@ncsu.edu (R.E.G.).

Notes
The authors declare no competing financial interest.

■ REFERENCES

(1) Mikos, A.; Bao, Y.; Cima, L.; Ingber, D.; Vacanti, J.; Langer, R. *J. Biomed. Mater. Res.* **1993**, *27*, 183−189.
(2) You, Y.; Lee, S.; Lee, S.; Park, W. *Mater. Lett.* **2006**, *60*, 1331−1333.
(3) Choi, S.; Lee, Y. S.; Joo, C. W.; Lee, S. G.; Park, J. K.; Han, K. *Electrochim. Acta* **2004**, *50*, 339−343.
(4) Zia, Q.; Ingolic, E.; Androsch, R. *Colloid Polym. Sci.* **2010**, *288*, 819−825.
(5) Gupta, V. B.; Kumar, S. *J. Appl. Polym. Sci.* **1981**, *26*, 1865−1876.
(6) Babatope, B.; Isaac, D. *Polymer* **1992**, *33*, 1664−1668.
(7) Richardson, H. H.; Thomas, A. C.; Carlson, M. T.; Kordesch, M. E.; Govorov, A. O. *J. Electron. Mater.* **2007**, *36*, 1587−1593.
(8) Srivastava, S.; Haridas, M.; Basu, J. *Bull. Mater. Sci.* **2008**, *31*, 213−217.
(9) Cong, H.; Radosz, M.; Towler, B. F.; Shen, Y. *Sep. Purif. Technol.* **2007**, *55*, 281−291.
(10) Roy, M.; Nelson, J.; MacCrone, R.; Schadler, L.; Reed, C.; Keefe, R. *IEEE Trans. Dielectr. Electr. Insul.* **2005**, *12*, 629−643.
(11) Liu, J.; Guo, T.; Yang, Y. *J. Appl. Phys.* **2002**, *91*, 1595−1600.
(12) Sershen, S. R.; Westcott, S. L.; Halas, N. J.; West, J. L. *J. Biomed. Mater. Res.* **2000**, *51*, 293−298.
(13) Alsawafta, M.; Badilescu, S.; Paneri, A.; Truong, V.; Packirisamy, M. *Polymers* **2011**, *3*, 1833−1848.
(14) Armentano, I.; Marinucci, L.; Dottori, M.; Balloni, S.; Fortunati, E.; Pennacchi, M.; Becchetti, E.; Locci, P.; Kenny, J. *J. Biomater. Sci., Polym. Ed.* **2011**, *22*, 541−556.
(15) Li, J.; Claude, J.; Norena-Franco, L. E.; Seok, S. I.; Wang, Q. *Chem. Mater.* **2008**, *20*, 6304−6306.
(16) Li, R.; Yao, D. *J. Appl. Polym. Sci.* **2008**, *107*, 2909−2916.
(17) Buchner, S.; Wiswe, D.; Zachmann, H. G. *Polymer* **1989**, *30*, 480−488.
(18) Jain, P. K.; Lee, K. S.; El-Sayed, I. H.; El-Sayed, M. A. *J. Phys. Chem. B* **2006**, *110*, 7238−7248.
(19) Wu, X.; Ming, T.; Wang, X.; Wang, P.; Wang, J.; Chen, J. *ACS Nano* **2009**, *4*, 113−120.
(20) Zhao, J.; Zhang, X.; Yonzon, C. R.; Haes, A. J.; Van Duyne, R. P. **2006**.
(21) Wybourne, M.; Hutchison, J.; Clarke, L.; Brown, L.; Mooster, J. *Microelectron. Eng.* **1999**, *47*, 55−57.
(22) Wybourne, M. N.; Clarke, L.; Yan, M.; Cai, S. X.; Brown, L. O.; Hutchison, J.; Keana, J. F. *Jpn. J. Appl. Phys.* **1997**, *36*, 7796−7800.
(23) Clarke, L.; Wybourne, M.; Yan, M.; Cai, S.; Brown, L.; Hutchison, J.; Keana, J. *J. Vac. Sci. Technol., B: Microelectron. Nanometer Struct.—Process., Meas., Phenom.* **1997**, *15*, 2925−2929.
(24) Berven, C.; Wybourne, M.; Clarke, L.; Longstreth, L.; Hutchison, J.; Mooster, J. *J. Appl. Phys.* **2002**, *92*, 4513−4517.
(25) Maier, S. A.; Atwater, H. A. *J. Appl. Phys.* **2005**, *98*, 011101−011101−10.
(26) Link, S.; El-Sayed, M. A. *Int. Rev. Phys. Chem.* **2000**, *19*, 409−453.
(27) Link, S.; El-Sayed, M. A. *Int. Rev. Phys. Chem.* **2000**, *103*, 409−453.
(28) Rashidi-Huyeh, M.; Palpant, B. *J. Appl. Phys.* **2004**, *96*, 4475−4482.
(29) Liu, C.; Li, B. Q.; Mi, C. C. *IEEE Trans. NanoBiosci.* **2009**, *8*, 271−280.
(30) Maity, S.; Wu, W.-C.; Tracy, J. B.; Bochinski, J. R.; Clarke, L. I. To be submitted.
(31) Link, S.; El-Sayed, M. *Int. Rev. Phys. Chem.* **2000**, *35*, 409−453.
(32) Zharov, V.; Lapotko, D. *IEEE J. Sel. Top. Quantum Electron.* **2005**, *11*, 733−751.
(33) Boyer, D.; Tamarat, P.; Cognet, L.; Orrit, M.; Lounis, B. *Manipulation Anal. Biomolecules, Cells Tissues* **2003**, *4962*, 121−125.
(34) Zharov, V.; Galitovsky, V.; Viegas, M. *Appl. Phys. Lett.* **2003**, *83*, 4897−4899.
(35) Boyer, D.; Tamarat, P.; Maali, A.; Lounis, B.; Orrit, M. *Science* **2002**, *297*, 1160−1163.
(36) Lapotko, D. *Opt. Express* **2009**, *17*, 2538−2556.
(37) Harris, N.; Ford, M.; Cortie, M. *J. Phys. Chem. B* **2006**, *110*, 10701−10707.
(38) Sershen, S.; Westcott, S.; West, J.; Halas, N. *Appl. Phys. B: Laser Opt.* **2001**, *73*, 379−381.
(39) Huang, X.; Jain, P. K.; El-Sayed, I. H.; El-Sayed, M. A. *Lasers in Medical Science* **2008**, *23*, 217−228.
(40) Takahara, J.; Yamagishi, S.; Taki, H.; Morimoto, A.; Kobayashi, T. *Opt. Lett.* **1997**, *22*, 475−477.
(41) Takahashi, H.; Niidome, T.; Nariai, A.; Niidome, Y.; Yamada, S. *Nanotechnology* **2006**, *17*, 4431−4435.
(42) Takahashi, H.; Niidome, T.; Nariai, A.; Niidome, Y.; Yamada, S. *Chem. Lett.* **2006**, *35*, 500−501.
(43) Chen, J. Y.; Wiley, B.; Li, Z. Y.; Campbell, D.; Saeki, F.; Cang, H.; Au, L.; Lee, J.; Li, X. D.; Xia, Y. N. *Adv. Mater.* **2005**, *17*, 2255−2261.
(44) Svaasand, L. O.; Gomer, C. J.; Morinelli, E. *Lasers Med. Sci.* **1990**, *5*, 121−128.
(45) Sershen, S. R.; Westcott, S. L.; Halas, N. J.; West, J. L. *J. Biomed. Mater. Res.* **2000**, *51*, 293−298.
(46) Radt, B.; Smith, T.; Caruso, F. *Adv. Mater.* **2004**, *16*, 2184−2189.
(47) Skirtach, A. G.; Antipov, A. A.; Shchukin, D. G.; Sukhorukov, G. B. *Langmuir* **2004**, *20*, 6988−6992.
(48) Maity, S.; Downen, L. N.; Bochinski, J. R.; Clarke, L. I. *Polymer* **2011**, *52*, 1674−1685.
(49) Maity, S.; Bochinski, J. R.; Clarke, L. I. *Adv. Funct. Mater.* **2012**, *22*, 5259−5270.
(50) Maity, S.; Kozek, K. A.; Wu, W.; Tracy, J. B.; Bochinski, J. R.; Clarke, L. I. *Part. Part. Syst. Charact.* **2013**, *30*, 193−202.
(51) Frens, G. *Nature (London), Phys. Sci.* **1973**, *241*, 20−22.
(52) Bur, A. J.; Vangel, M. G.; Roth, S. *Appl. Spectrosc.* **2002**, *56*, 174−181.
(53) Strobl, G. R. *The Physics of Polymers: Concepts for Understanding Their Structures and Behavior*; Springer: Berlin, 2007.
(54) Chatterjee, A. M.; Price, F. P.; Newman, S. *J. Polym. Sci., Polym. Phys. Ed.* **1975**, *13*, 2391−2400.
(55) Stadlbauer, M.; Eder, G.; Janeschitz-Kriegl, H. *Polymer* **2001**, *42*, 3809−3816.
(56) Tribout, C.; Monasse, B.; Haudin, J. *Colloid Polym. Sci.* **1996**, *274*, 197−208.
(57) Wieczorek, W.; Such, K.; Florjanczyk, Z.; Stevens, J. *J. Phys. Chem.* **1994**, *98*, 6840−6850.
(58) Kim, G.; Wutzler, A.; Radusch, H.; Michler, G. H.; Simon, P.; Sperling, R. A.; Parak, W. *J. Chem. Mater.* **2005**, *17*, 4949−4957.
(59) Lin, H.; Freeman, B. D. *J. Membr. Sci.* **2004**, *239*, 105−117.
(60) Coutts-Lendon, C.; Koenig, J. L. *Appl. Spectrosc.* **2005**, *59*, 976−985.
(61) Chan, C. M.; Li, L. *Intrinsic Mol. Mobility Toughness Polym. II* **2005**, 1−41.
(62) Roberts, R. *Polymer* **1969**, *10*, 117−125.
(63) Yeh, G. S.; Hosemann, R.; Loboda-Čačković, J.; Čačković, H. *Polymer* **1976**, *17*, 309−318.
(64) Massa, M. V.; Dalnoki-Veress, K.; Forrest, J. *Eur. Phys. J. E* **2003**, *11*, 191−198.
(65) Chen, E.; Jing, A. J.; Weng, X.; Huang, P.; Lee, S.; Cheng, S. Z.; Hsiao, B. S.; Yeh, F. *Polymer* **2003**, *44*, 6051−6058.

(66) He, Y. Q.; Liu, S. P.; Kong, L.; Liu, Z. F. *Spectrochim. Acta, Part A* **2005**, *61*, 2861−2866.

(67) Wang, H.; Keum, J. K.; Hiltner, A.; Baer, E.; Freeman, B.; Rozanski, A.; Galeski, A. *Science* **2009**, *323*, 757−760.

(68) Snétivy, D.; Vancso, G. J. *Polymer* **1992**, *33*, 432−433.

(69) Sınmazçelik, T.; Yılmaz, T. *Mater. Des.* **2007**, *28*, 641−648.

(70) Zhokhavets, U.; Erb, T.; Gobsch, G.; Al-Ibrahim, M.; Ambacher, O. *Chem. Phys. Lett.* **2006**, *418*, 347−350.

(71) Painter, P. C.; Coleman, M. M. *Essentials of Polymer Science and Engineering*; DEStech Publications, Inc.: Lancaster, PA, 2008.

(72) Cheng, S.; Chen, J.; Wu, S.; Zhang, A.; Yandrasits, M.; Zhuo, Q.; Quirk, R. *Cryst. Polym.* **1993**, *405*, 51−62.

(73) Dreezen, G.; Koch, M. H. J.; Reynaers, H.; Groeninckx, G. *Polymer* **1999**, *40*, 6451−6463.

(74) Pearce, R.; Vancso, G. *Macromolecules* **1997**, *30*, 5843−5848.

(75) Liao, C.; Ye, W. *Electrochim. Acta* **2004**, *49*, 4993−4998.

(76) Srithep, Y.; Nealey, P.; Turng, L. *Polym. Eng. Sci.* **2013**, *53*, 580−588.

(77) Djokovic, V.; Dramicanin, M.; Kostoski, D.; Dudic, D. *Trends Adv. Mater. Processes* **2000**, *352*, 195−200.